Science Advances
AAAS

Supplementary Materials for

Melanoma progression and prognostic models drawn from single-cell, spatial maps of benign and malignant tumors

Nick R. Love *et al.*

Corresponding author: Maija Kiuru, mkiuru@ucdavis.edu

Sci. Adv. **10**, eadm8206 (2024)
DOI: 10.1126/sciadv.adm8206

The PDF file includes:

Other Supplementary Material for this manuscript includes the following:

Supplementary Text

Explanatory detail of RNA-SMI technique

The NanoString® CosMx™ RNA Spatial Molecular Imaging (RNA-SMI) technique utilizes anti-sense oligonucleotide probes conjugated to unique fluorophore-reacting "readout" domains (Fig. 1A). Each gene is targeted at 5 separate locations along the 5' to 3' axis to increase signal-to-noise ratio and reduce false positives. After probe hybridization, the readout domain is cyclically exposed to fluorophores and plexed to allow simultaneous detection of ~1000 cancer-associated genes (Data S3 and Data S7).

After RNA imaging, slides are stained for nuclei (DAPI staining) and protein (immunohistochemistry), which facilitates computer automated 2-dimensional (2D) cell segmentation. This creates a 2D cellular "map" atop which RNA transcripts (1 dimensional points) can be arbitrarily sized, colored, and superimposed (Fig. 1A). Nuclear, mitochondrial, or organelle-localized mRNA transcripts can be concurrently visualized within their respective compartments, bestowing RNA-SMI "subcellular" resolution.

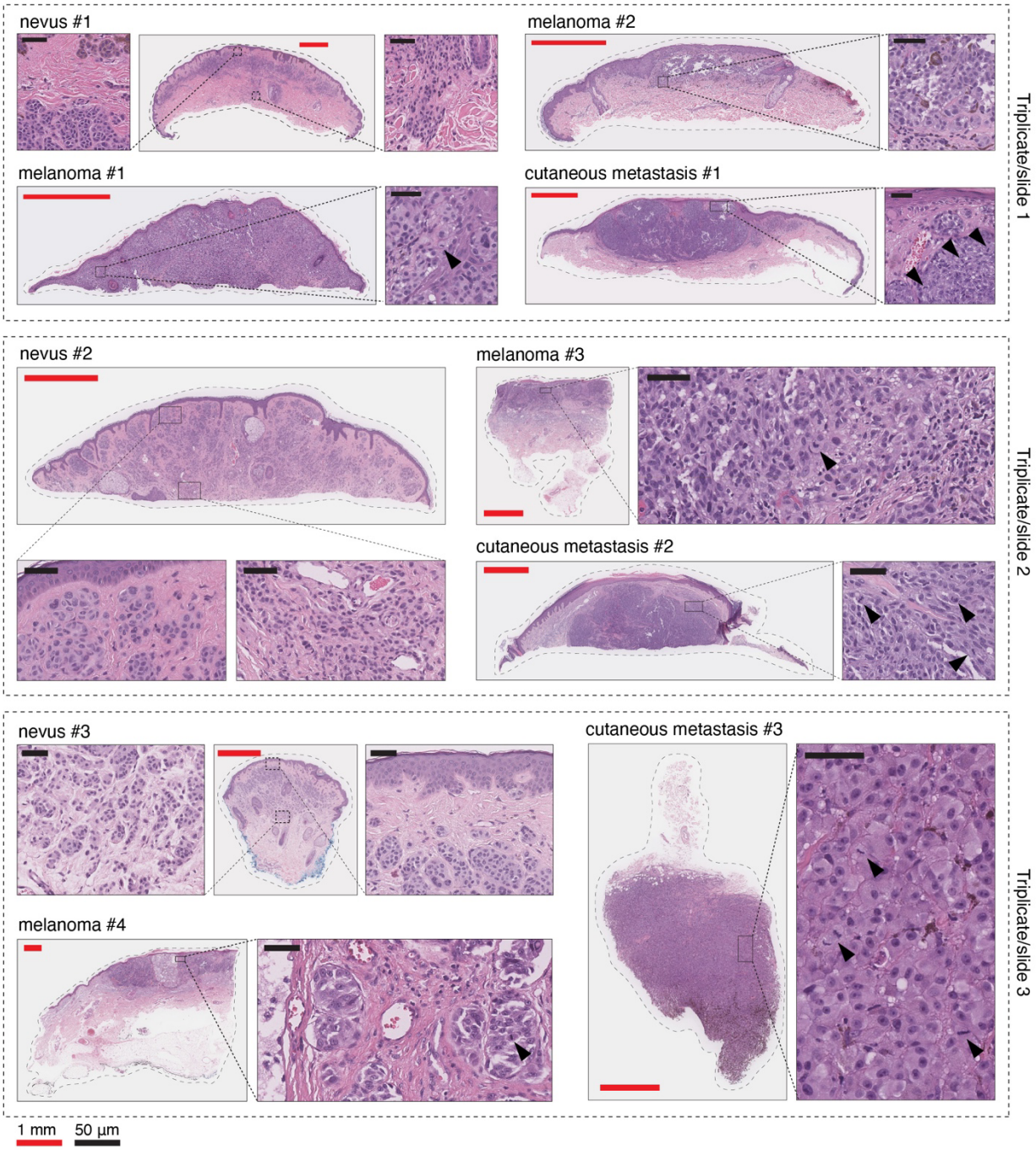

Fig. S1. Melanocytic tumors analyzed using RNA-SMI generate a dataset that encompasses 203,472 cells. Magnified insets highlight diagnostic areas of each respective tumor. Closed black arrows indicate mitotic cells. Clinical history of each neoplasm outlined in Data S1.

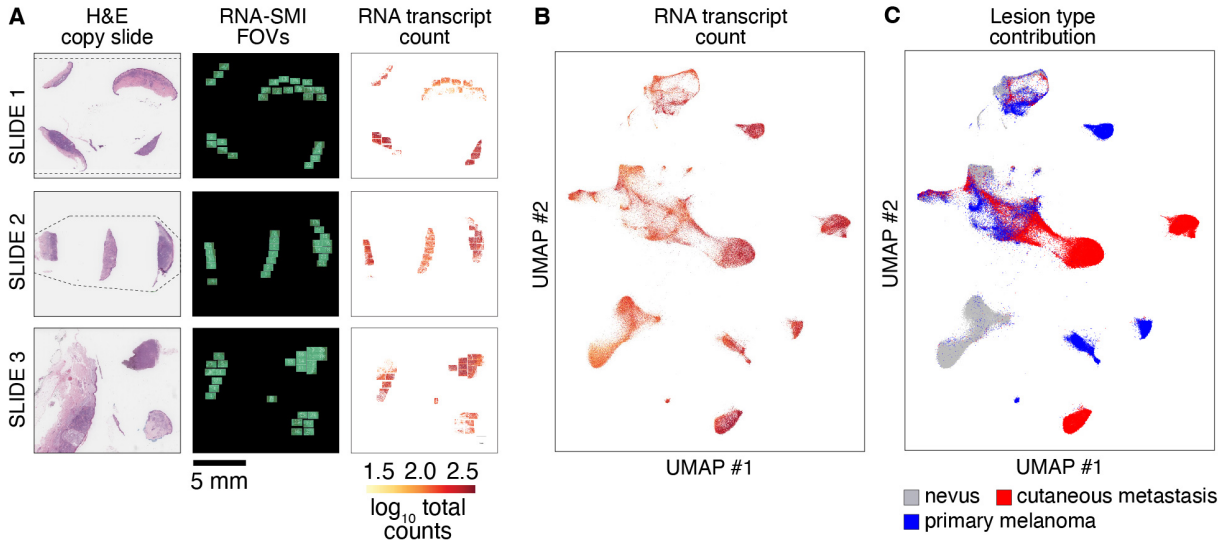

Fig. S2. H&E of slide portion available for RNA-SMI, microscopic Field of Views (FOVs), and distribution of transcript counts in 2D space and in UMAP projection. (A) Left panels show the respective H&E copy slide generated for Slides 1-3 that were subjected to RNA-SMI. Namely, the left panels show the central portion of the glass slide that has the capacity to be imaged by RNA-SMI. The middle panels (which are separate sections than the left most H&E copy slides) show how the RNA-SMI microscope FOVs (0.7 mm x 0.9 mm) were used to tile image the neoplasms in the left most panels (highlighted in fig. S1). Right panels show the subsequent number of gene transcripts detected in each area of the neoplasm FOVs that, overall, demonstrate a relative even distribution of transcript detection amongst the neoplasms. **(B)** Transcript count per cell in UMAP projection, with similar color key as (A). **(C)** Location of cells of nevus, primary melanoma, and cutaneous metastases within the UMAP plots.

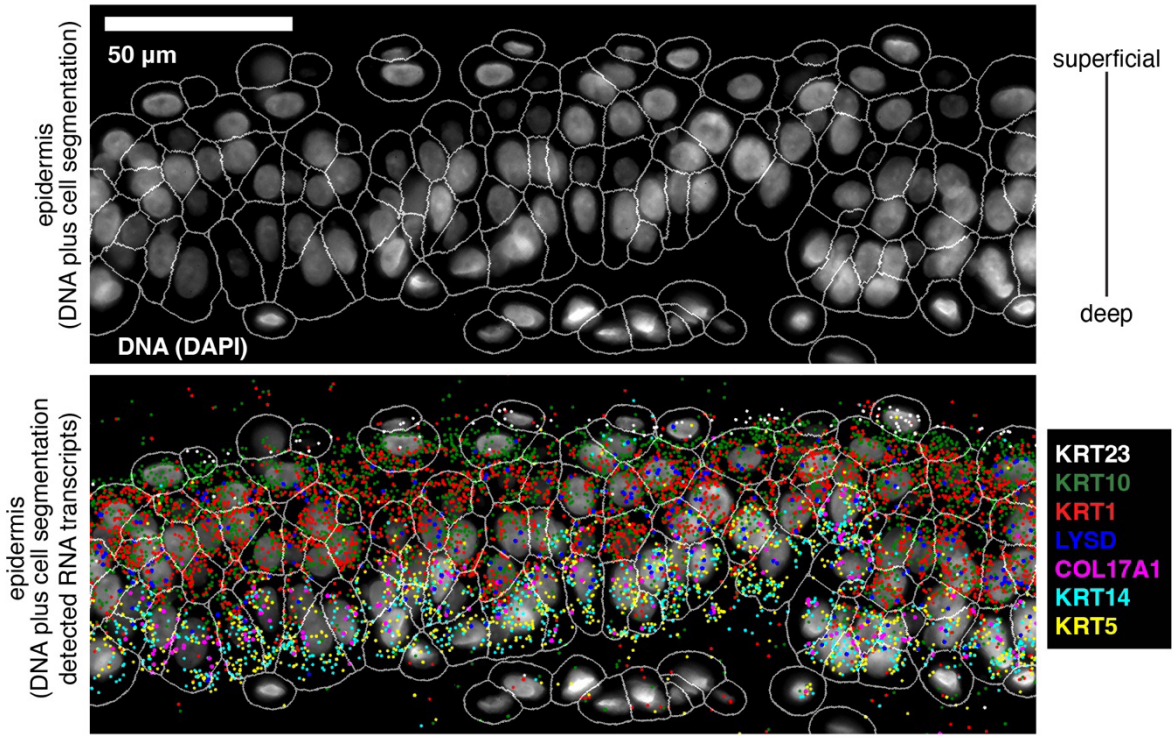

Fig. S3. Superficial to deep epidermal gene expression patterns. The panels show a section of epidermis in the axis indicated at the right. Top panel show DNA (DAPI staining) and subsequent *in silico* cell segmentation (white borders). Bottom panel shows the addition of detected RNA transcripts for the genes listed at bottom right. Collectively, the panels show the correct localization of basal epidermal layer expression of *COL17A*, *KRT14*, and *KRT5* versus more superficial layer expression of *KRT23*, *KRT10*, *KRT1*, and *LYSD*.

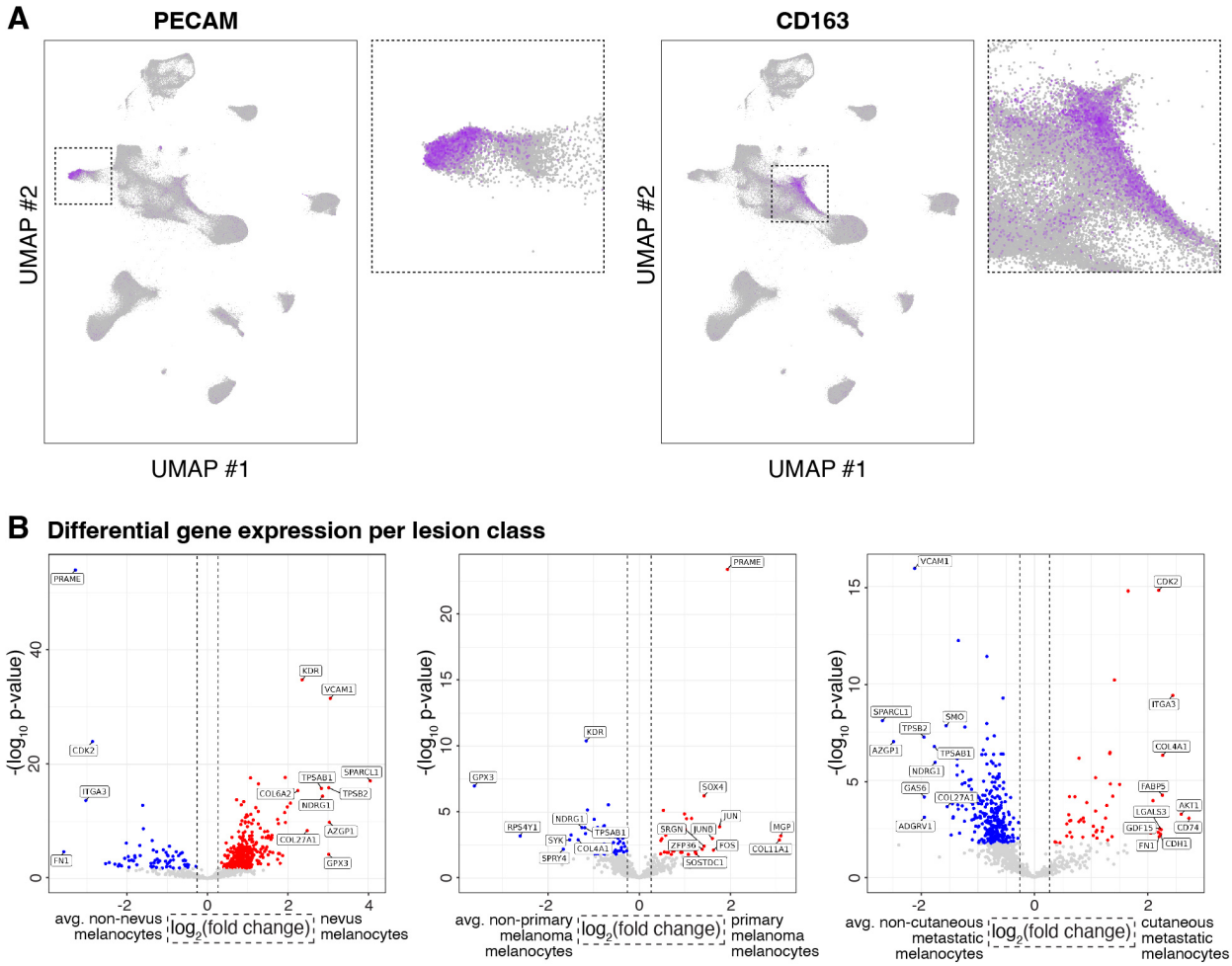

Fig. S4. Cell-type specific candidate gene UMAPs. (A) Left panel shows putative vascular endothelial cells that express *PECAM* highlighted in purple, inset magnified as shown. Right panel shows putative monocytes/macrophages that express *CD163* highlighted in purple, inset magnified as shown. **(B)** The volcano plots show differential gene expression of lesion specific melanocytes (indicated on the X-axis) versus the average expression of remaining melanocytes. For instance, the left most panel shows genes with differential expression in nevus-type melanocytes (red) versus the average expression of primary melanoma-type and cutaneous metastasis-type melanocytes (blue). The center panel shows genes with differential expression in primary melanoma-type melanocytes (red) versus the average expression of nevus-type and cutaneous metastasis-type melanocytes (blue). The right panel shows genes with differential expression in cutaneous metastasis-type melanocytes (red) versus the average expression of nevus-type and primary melanoma-type melanocytes (blue). Points are colored red or blue if below FDR threshold of 0.05.

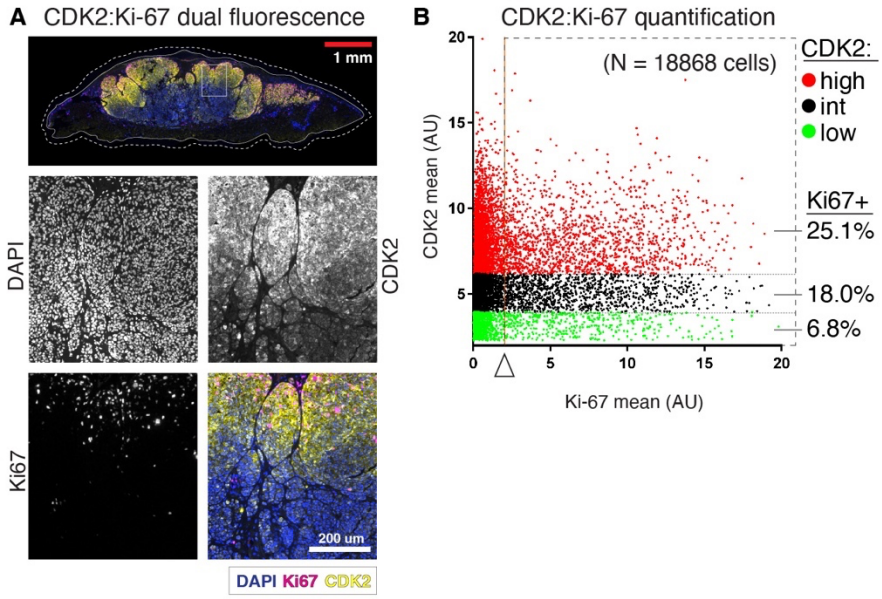

Fig. S5. CDK2:Ki67 dual fluorescence and quantification. **(A)** Panel show the CDK2 (shown in yellow), Ki-67 (shown in pink), and DNA (DAPI staining, shown in blue) of the cutaneous metastatic melanoma highlighted in Fig. 2E. The stains show increased Ki-67 positivity in aggregates that have greater CDK2 staining. **(B)**. Quantification of individual cell CDK2:Ki-67 mean fluorescence (in arbitrary units, AU) of the 18868 tumoral cells analyzed from (A). Cells were evenly stratified into high, intermediate (int), and low expressing tertiles, as shown in the color key the right. Corresponding Ki-67 positivity rate for each tertile is shown at the bottom right. The graphic shows how increased CDK2 fluorescence correlates with increased chance of being Ki-67 positive (as defined by having fluorescence that passes the open white arrowhead).

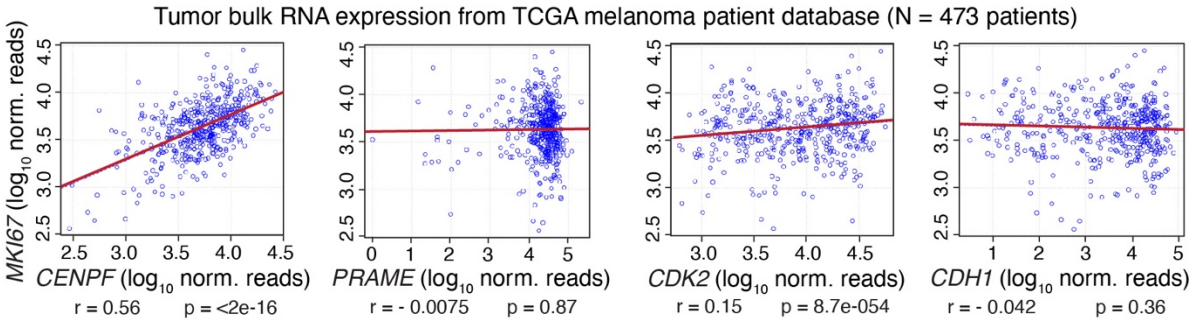

Fig. S6. Correlation of *MKI67* with *CENPF*, *PRAME*, *CDK2*, and *CDH1* using tumor bulk RNA expression values from TCGA melanoma patient database. Respective r-values (Pearson's product moment correlation coefficient) and p-values are shown below each respective plot.

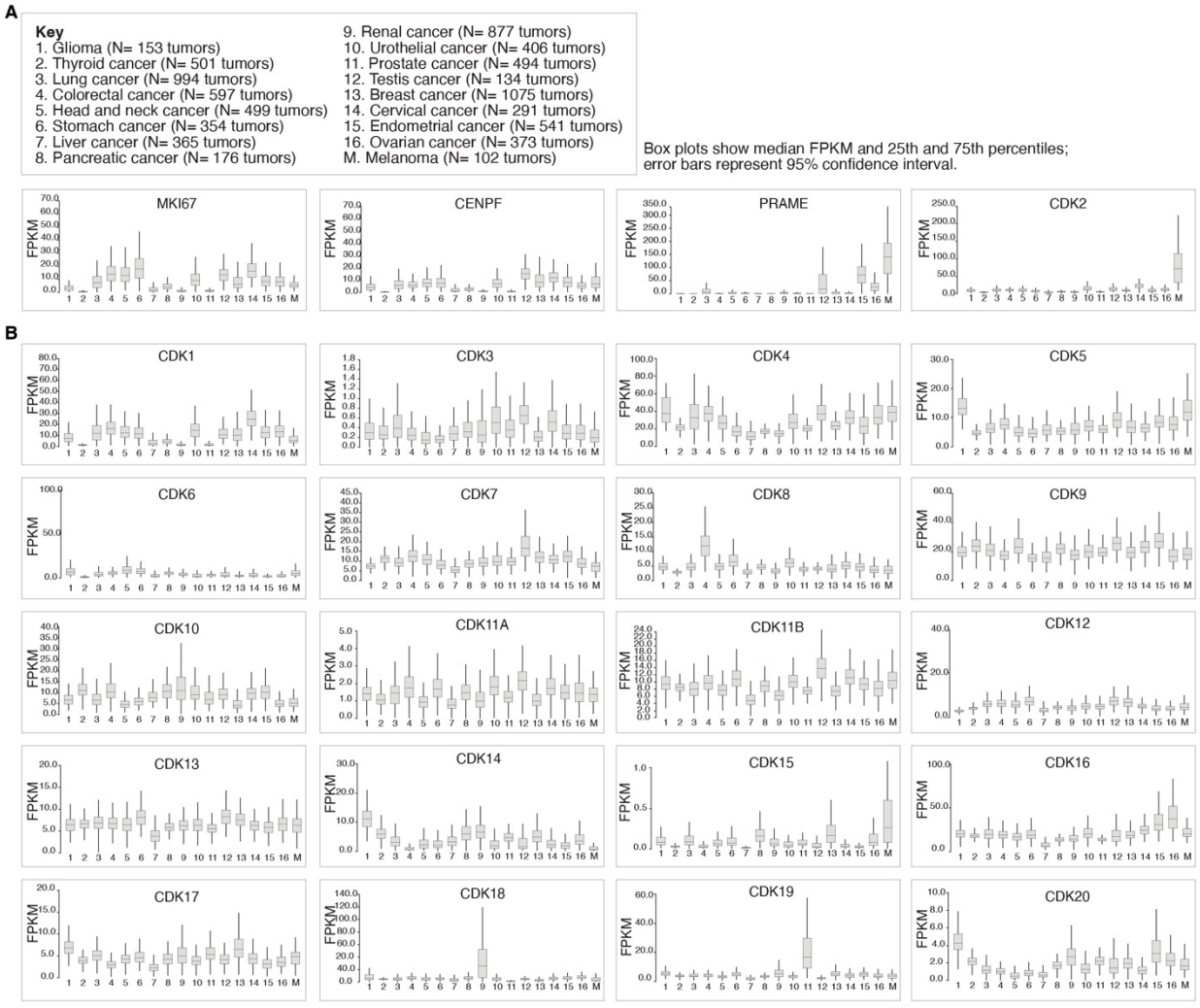

Fig. S7. Expression of *MKI67, CENPF, PRAME*, and *CDK*s in various cancer types. (A) Top panel shows key and N values of the different cancers show in the individual panels. Bottom four panels show expression of *MKI67, CENPF, PRAME*, and *CDK2*, which collectively, show the comparative increase in expression of *CDK2* in melanoma versus other cancer types. **(B)** Panels show expression of *CDK* family, which collectively with (A), show that *CDK2* is the only CDK that shows the comparative increased in melanoma versus other cancer types. These data were obtained from the Human Protein Atlas (www.proteinatlas.org) on May 12th 2023.

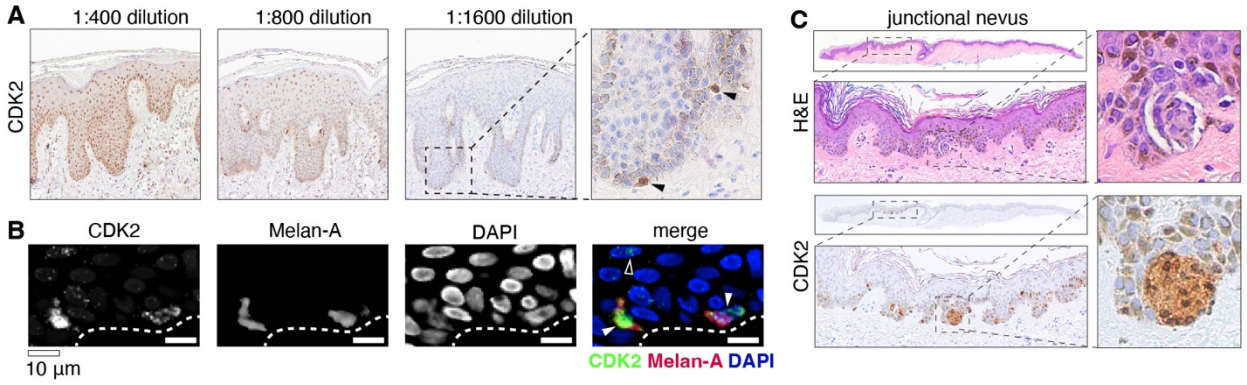

Fig. S8. Expression of CDK in dermal-epidermal benign melanocytes and in melanocytic nests of junctional nevus. (A) Serial dilutions with a CDK2 monoclonal antibody highlight dermal-epidermal melanocytes (closed black arrow heads). **(B)** Panels show co-localization of CDK2 and melanocytic marker Melan-A in melanocytes (closed white arrow heads) in the basal layer of the epidermis. White dashed line shows bottom edge of basal layer of epidermis. Open white arrowhead shows sparse staining of CDK2 in keratinocytes. **(C)** Panel shows show expression of CDK2 in the nest of a benign junctional nevus.

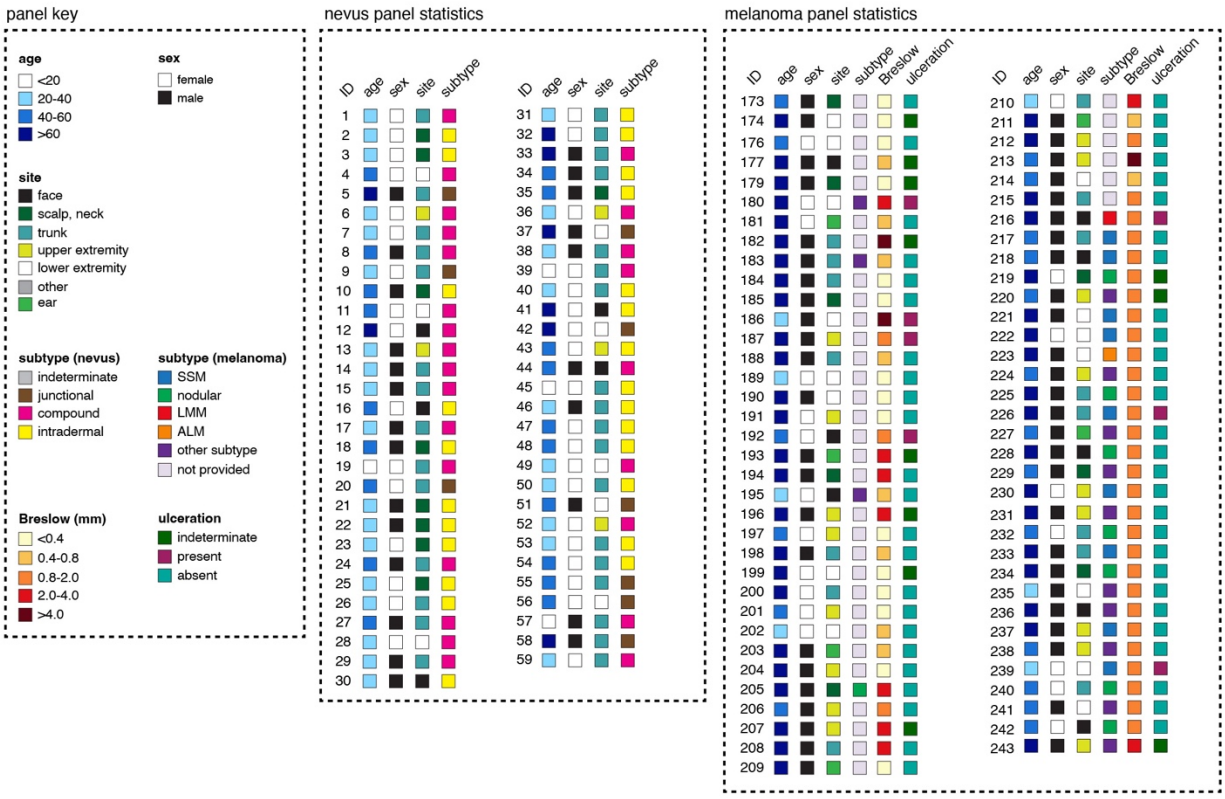

Fig. S9. Demographic and histologic characteristics of nevus and melanoma tumor panel.

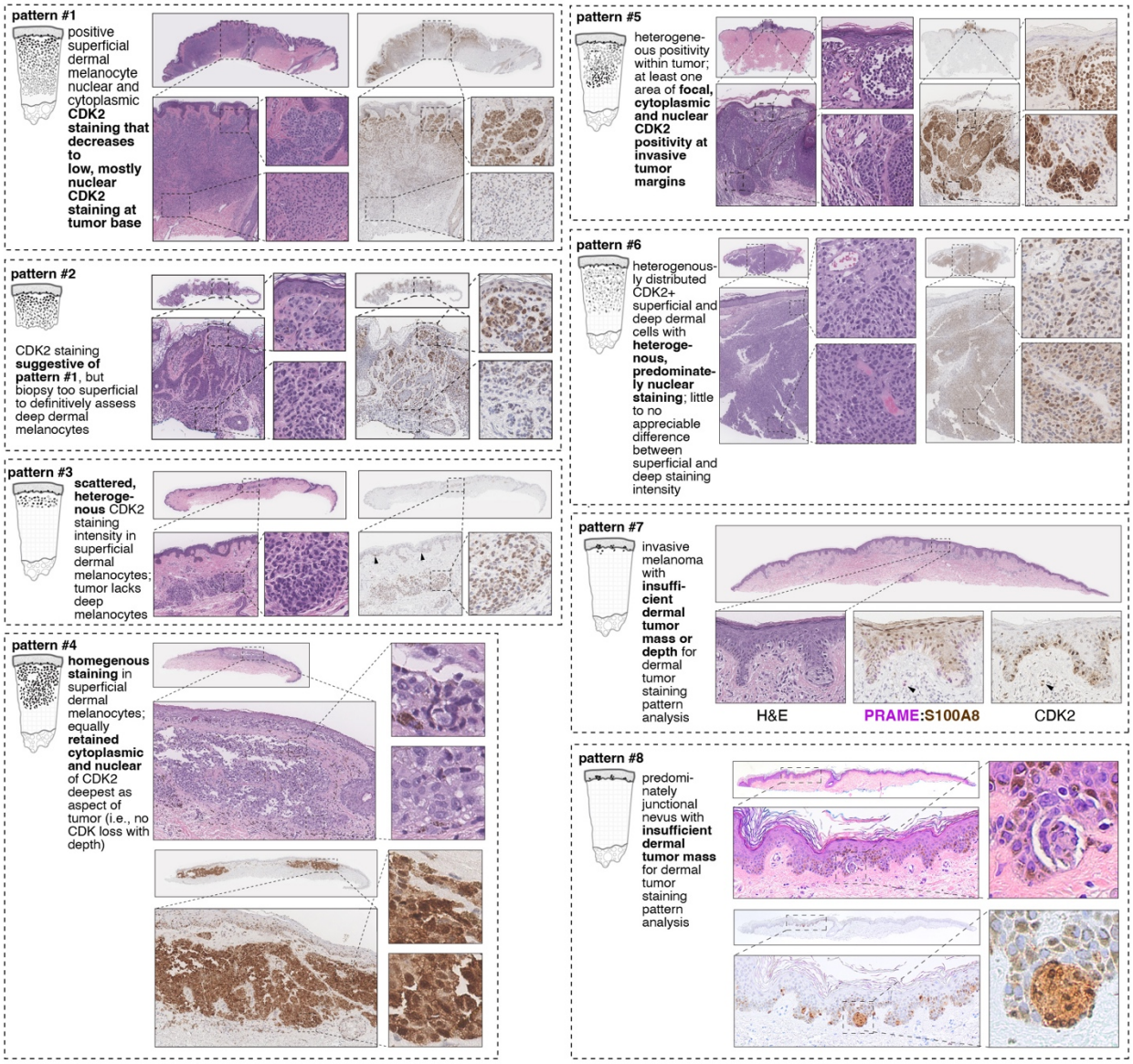

Fig. S10. Representative CDK2 expression patterns. Note, pattern #8 show a predominately junctional nevus, the micrographs of which were also shown in fig. S8.

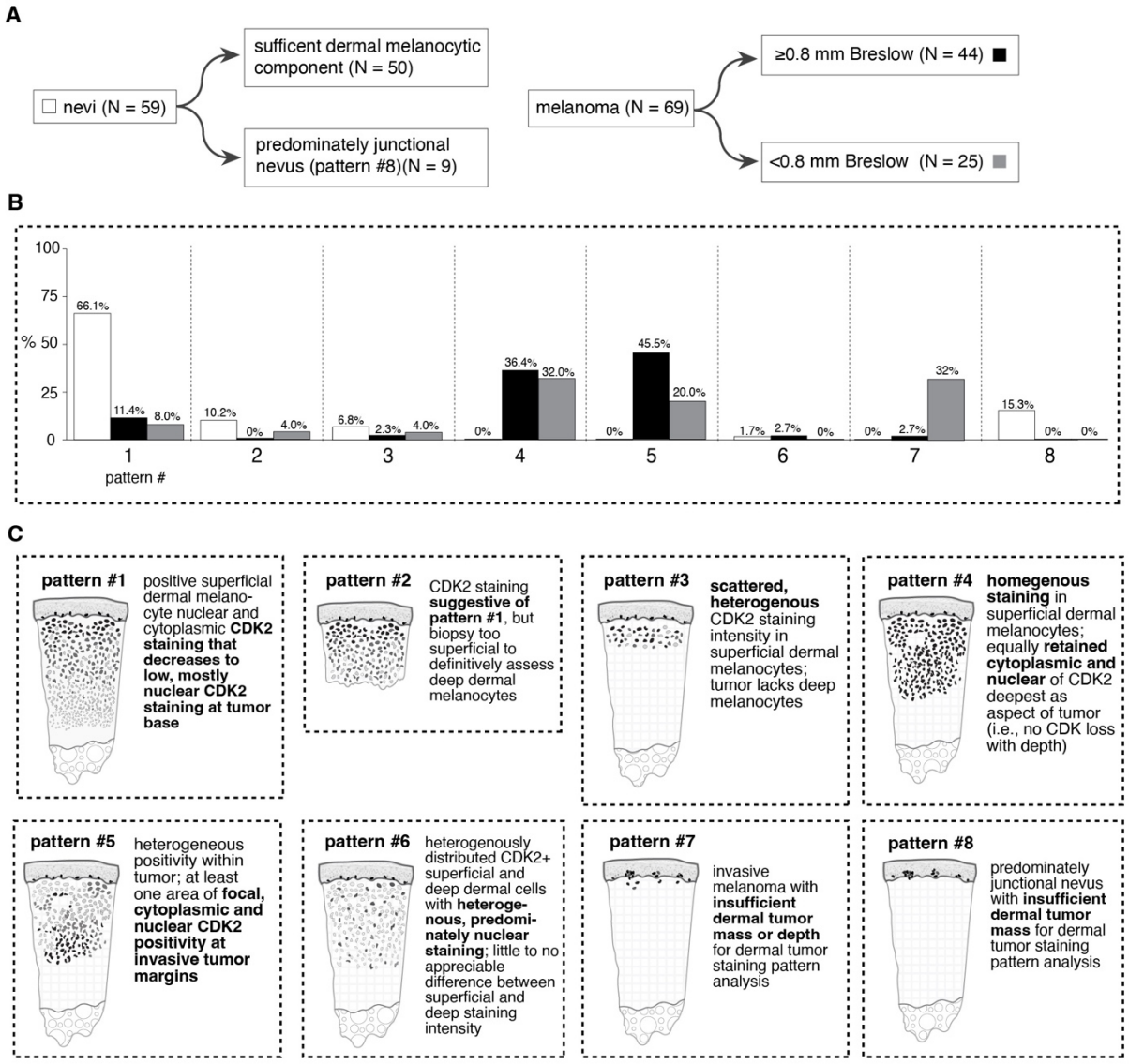

Fig. S11. Scoring of tumor panel CDK2 expression patterns. (A) The schematic shows numerical breakdown of tumor panel by histology (nevus) or Breslow depth (melanoma). **(B)** Bar graphs show the qualitative scoring results of the nevus and melanoma tumor panel, the scoring criteria of which is shown in **(C)** for convenience (originally shown in fig. S10).

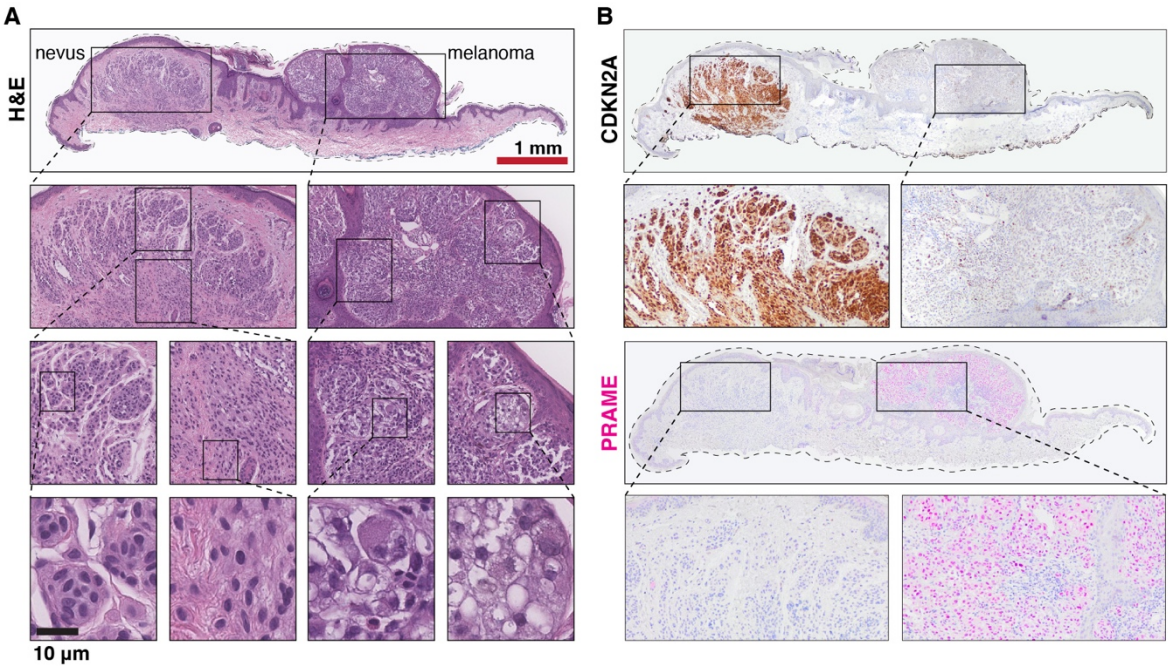

Fig. S12. Protein validation of combined nevus-melanoma neoplasm. (A) Panels show characteristic histopathology of nevus (left) and melanoma (right) portions of the heterogenous neoplasm. The nevus portion is characterized by ordered, bland appearing melanocytes that exhibit gradual reductions in cytoplasm at the deep aspect of the proliferation. The melanocytes of the melanoma portion show increased nuclear pleomorphism and epithelioid cytology. **(B)** Panels show retained and comparatively greater expression of CDKN2A (also known as p16) in nevus portion of neoplasm versus the increased expression of PRAME in the melanoma portion of the neoplasm.

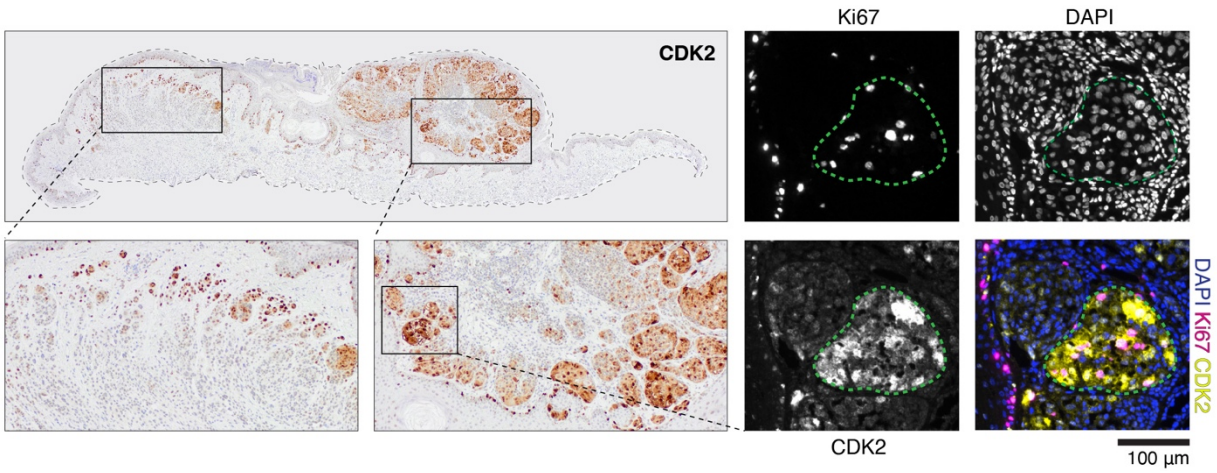

Fig. S13. Increased CDK2 and Ki-67 expression in melanoma tissue aggregate. The panels show CDK2 staining and CDK2:Ki-67 dual immunofluorescence analysis of the heterogenous neoplasm highlighted in Fig. 4. The green dotted line highlights an aggregate with increased CDK2 and Ki-67 staining.

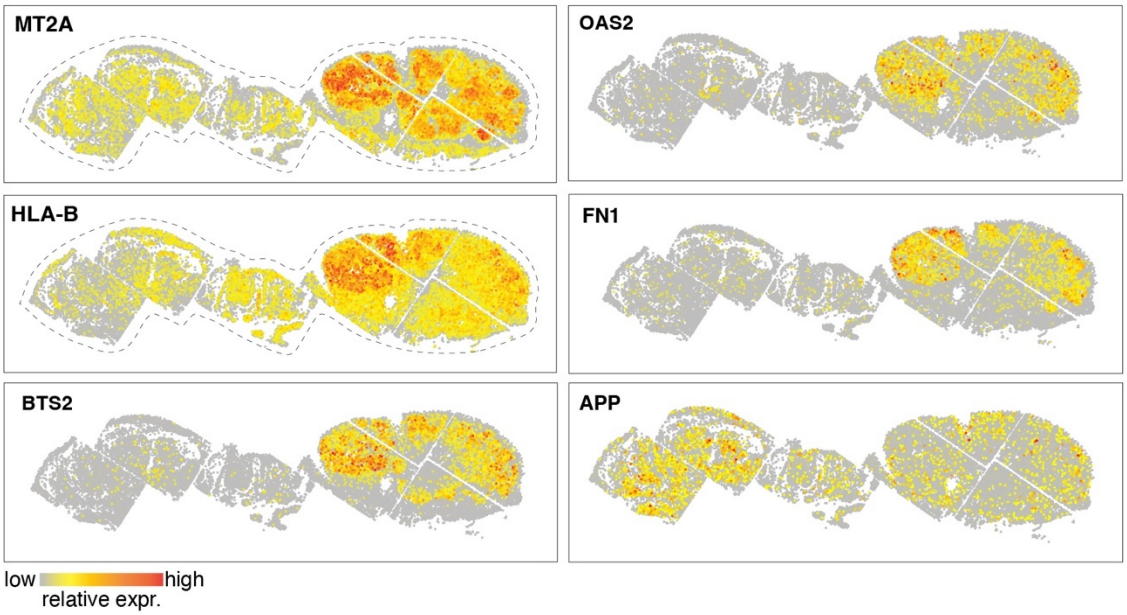

Fig. S14. Spatial expression patterns of melanoma-nevus heterogenous neoplasm. The panels show a selection of gene targets identified in the differential and spatial analyses featured in Fig. 4.

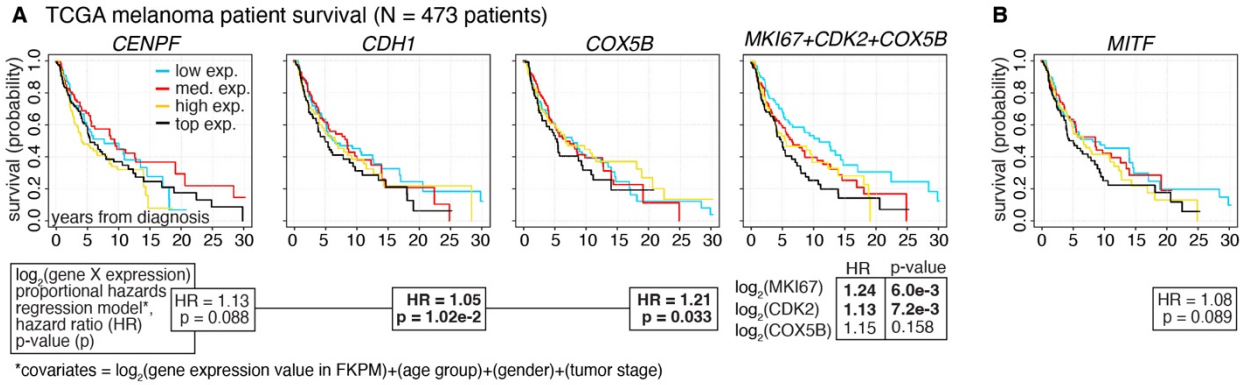

Fig. S15. Kaplan-Meier and Cox Regression analyses. (A) Panels show Kaplan-Meier curves of the genes shown above after dividing patients into low, medium (med.) high, and top expression quartiles based on normalized expression levels. **(B)** Panel shows Kaplan-Meier curves after dividing patients into quartiles based on *MITF* expression levels. For the Kaplan-Meier curves in A and B, the results of Cox (proportional hazards) regression model and p-values are shown below.

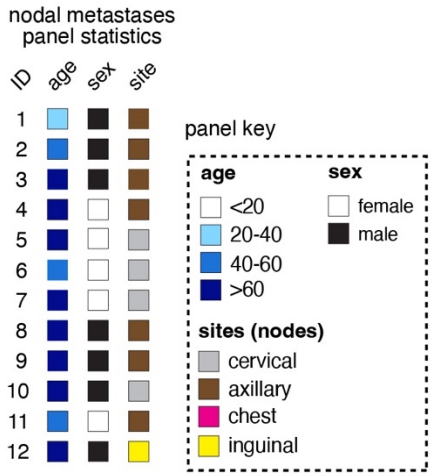

Fig. S16. Patient and anatomic characteristics in melanoma nodal metastases panel

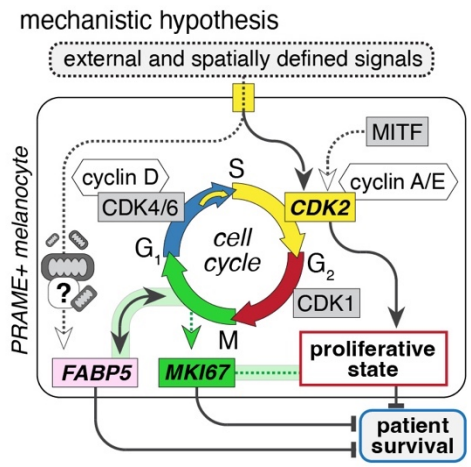

Fig. S17. Working model that hypothesizes how *MKI67, CDK2*, and *FABP5* expression may mechanistically converge within the PRAME+ malignant melanocyte to affect patient survival.

Data S1. (Data_Supplement.xls, Tab 1)
Brief clinical summary of melanocytic neoplasms shown in Fig S1 that are highlighted in Figures 1-3.

Data S2. (Data_Supplement.xls, Tab 2)
DNA mutations revealed during the clinical workup of the cutaneous metastases shown in Fig S1 that are highlighted in Figures 1-2.

Data S3. (Data_Supplement.xls, Tab 3)
List of gene probes utilized in initial dataset that analyzed the 203,472 cells highlighted in Figures 1-3.

Data S4. (Data_Supplement.xls, Tab 4)
Gene detection and segmentation statistics of RNA-SMI analysis of 203,472 cells highlighted in Figures 1-3.

Data S5. (Data_Supplement.xls, Tab 5)
List of genes within Leiden clustering heatmap shown in Figure 2. Bottom portion shows average number of transcripts detected per cell per cluster (shown in Figure 2B).

Data S6. (Data_Supplement.xls, Tab 6)
Lee's L spatial clustering groups (Top 75 genes).

Data S7. (Data_Supplement.xls, Tab 7)
List of gene probes utilized as well as the gene detection and segmentation statistics of RNA-SMI analysis of dataset that analyzed the 84,312 cells highlighted in Figure 4.